HEALTH AND MEDICINE

Microneedle-mediated gene delivery for the treatment of ischemic myocardial disease

Hongpeng Shi[1]*, Tong Xue[2]*, Yang Yang[3], Chenyu Jiang[1], Shixing Huang[1], Qi Yang[1], Dong Lei[4], Zhengwei You[4], Tuo Jin[2], Fei Wu[2†], Qiang Zhao[1†], Xiaofeng Ye[1†]

Cardiovascular disorders are still the primary cause of mortality worldwide. Although intramyocardial injection can effectively deliver agents to the myocardium, this approach is limited because of its restriction to needle-mediated injection and the minor retention of agents in the myocardium. Here, we engineered phase-transition microneedles (MNs) coated with adeno-associated virus (AAV) and achieved homogeneous distribution of AAV delivery. Bioluminescence imaging revealed the successful delivery and transfection of AAV-luciferase. AAV–green fluorescent protein–transfected cardiomyocytes were homogeneously distributed on postoperative day 28. AAV–vascular endothelial growth factor (VEGF)–loaded MNs improved heart function by enhancing VEGF expression, promoting functional angiogenesis, and activating the Akt signaling pathway. The results indicated the superiority of MNs over direct muscle injection. Consequently, MNs might emerge as a promising tool with great versatility for delivering various agents to treat ischemic myocardial disease.

INTRODUCTION

The American Heart Association has stated that cardiovascular disease (CVD) is the primary cause of mortality worldwide, leading to more than 17.3 million deaths per year; the number of deaths is estimated to exceed 23.6 million by 2030 (*1*). Thus, all potential treatment strategies to preserve left ventricle (LV) function by limiting infarct expansion and alleviating adverse remodeling are currently being investigated (*2*). To date, various injectable agents, including biomaterials, cells, genes, and proteins (*3*–*7*), have been studied and shown to have various advantages. Direct intramyocardial delivery of agents through myocardial transfection in the ischemic regions where vascular delivery procedures were excluded and the systemic administration of vectors might pose potential hazards following the procedures of myocardial revascularization was suitable (*8*). However, the effects of intramyocardially delivered therapeutics are restricted to the site of injection (*9*–*11*). Another major drawback is the minor myocardial retention of injected agents. Previous reports have demonstrated that few injected cells are retained in injured hearts, which is one of the principal reasons for the failure of cell therapy for myocardial repair (*12*, *13*). On the other hand, all body tissues can be exposed to drugs if they accidently enter the left ventricular cavity, which can reduce therapeutic efficacy and contribute to unexpected results. Therefore, the current limitations associated with this strategy must be mitigated. Cardiac gene transfer has been considered to be a promising therapeutic tool in the field of cardiology (*14*, *15*). Adeno-associated virus (AAV)–9, a serotype with high cardiac tropism, persistent transgene expression, and low pathogenicity, has also been applied for cardiac gene therapy (*16*). Transgenic expression of AAVs starts from 5 to 7 days after administration, and remarkably elevated viral transfection efficiency is achieved at weeks 2 to 3. Delivered vectors continue to express their transgenes for 6 to 12 months in vivo (*17*, *18*). AAV-mediated gene expression in vivo declines with time due to promoter shutoff and loss of AAV-transduced cells and AAV particles (*19*).

Microneedles (MNs) are an array of small needles, up to 1 mm in length, that provide secure channels for the passage of therapeutic substances (*2*, *20*), especially macromolecules, without causing skin injury or pain; these macromolecules include nucleic acids in the form of genes (*21*), vaccines (*22*), and proteins (*23*–*25*). The precise and efficient transfusion and homogeneous distribution of therapeutic agents delivered via MNs make MN-mediated delivery a promising new administration method for ischemic heart disease (IHD) treatment. In this study, we fabricated phase-transition MNs (PTMs) and studied their properties as well as their safety and practicality for experimental application. A schematic illustrating the overall study design using AAV-harboring MNs (MN-AAV) is shown in Fig. 1A. Figure 1B represents our practice for the application of MNs to deliver therapeutic agents via endoscopy assisted microthoracotomy surgery. A series of endoscopic images demonstrate the in vivo application of MNs to deliver therapeutic agents to the rat heart as shown in Fig. 1C. MNs loaded with fluorescent fluorescein isothiocyanate (FITC)–labeled AAV (MN-FITC-AAV) and AAV containing the luciferase coding sequence (MN-AAV-LUC) enabled successful therapeutic agent delivery and gene transfection of target heart regions. AAV–green fluorescent protein (GFP)–loaded MNs (MN-AAV-GFP) enabled fine distribution of AAV particles, presenting an advantage over direct injection (DI), after which positive cells were limited in location to the injection site in vivo. Thus, MN-AAV, which allow agents to be burst-released, can achieve even distributions of agents at the target myocardium rather than confining the agents to the site of administration. Heart performance and histological examinations showed that MNs loaded with AAV vector–encoding vascular endothelial growth factor gene (MN-AAV-VEGF) could improve cardiac function, reduce scar size, ameliorate adverse remodeling, and elevate myocardial perfusion in a rat model of myocardial infarction (MI). MN-mediated gene therapy showed

[1]Department of Cardiac Surgery, Ruijin Hospital, Shanghai Jiao Tong University School of Medicine, Shanghai 200025, P. R. China. [2]School of Pharmacy, Shanghai Jiao Tong University, Shanghai 200240, P. R. China. [3]Department of Cardiothoracic Surgery, Xinhua Hospital, Shanghai Jiao Tong University School of Medicine, Shanghai 200092, P. R. China. [4]State Key Laboratory for Modification of Chemical Fibers and Polymer Materials, International Joint Laboratory for Advanced Fiber and Low-Dimension Materials, College of Materials Science and Engineering Donghua University, Shanghai 201620, P. R. China.
*These authors contributed equally to this work.
†Corresponding author. Email: xiaofengye@hotmail.com (X.Y.); zq11607@rjh.com.cn (Q.Z.); feiwu@sjtu.edu.cn (F.W.)

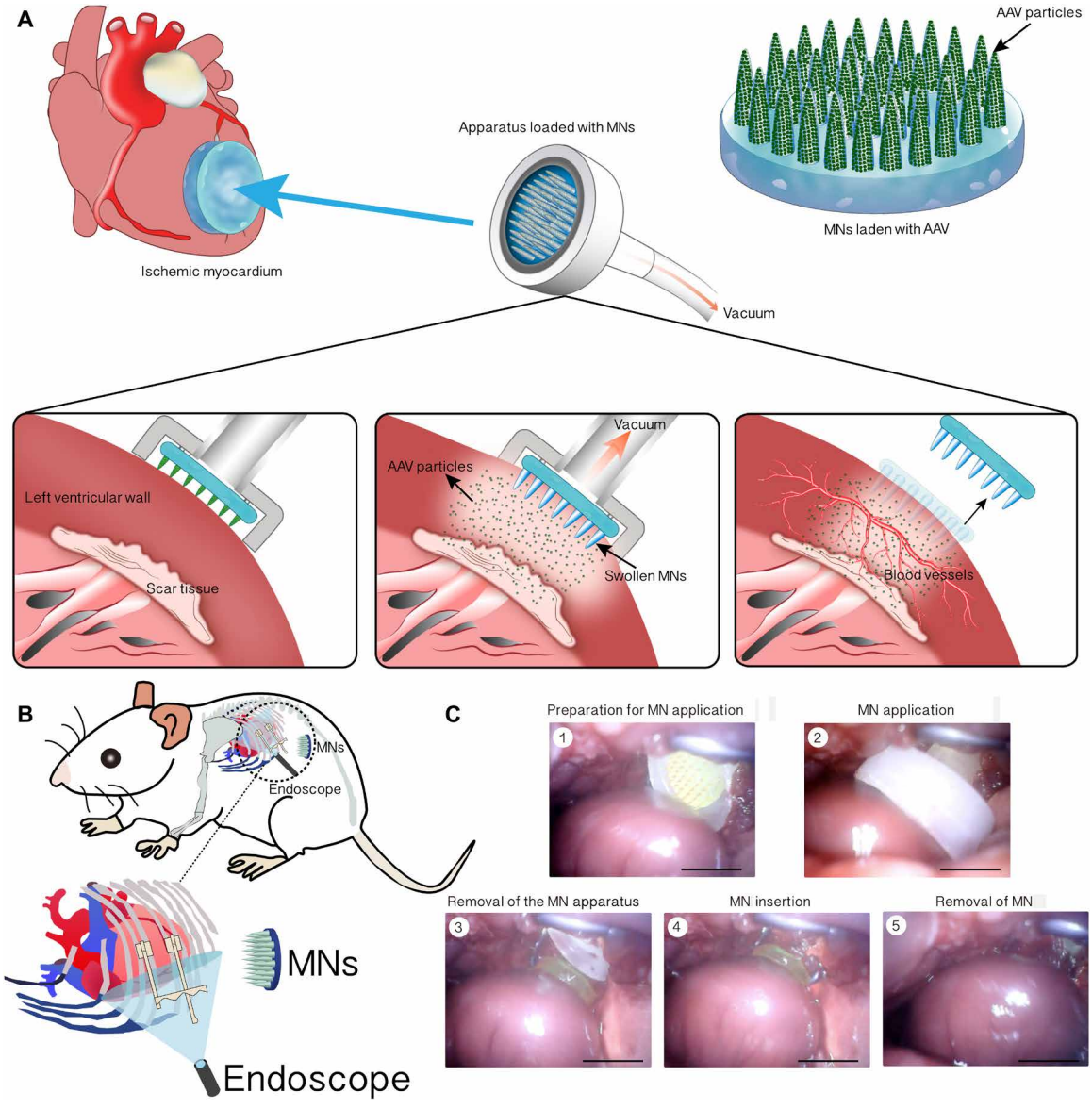

Fig. 1. Schematic showing the overall study design using MN-AAV. (**A**) Ischemic hearts were administered MN-AAV with the assistance of a customized apparatus. The MNs swelled following application; consequently, the therapeutic agents were burst-released into precise regions to ameliorate cardiac dysfunction through angiogenic effects. (**B**) Diagram of our practice for the application of the MNs to rat heart via endoscopy assisted microthoracotomy surgery. (**C**) A series of endoscopic images demonstrating the application of MNs for delivery of therapeutic agents to a rat heart. Scale bars, 600 μm. Photo credits: Hongpeng Shi, Department of Cardiac Surgery, Ruijin Hospital, Shanghai Jiao Tong University School of Medicine.

distinct superiority over DI and may therefore provide an alternative, minimally invasive therapeutic option for heart diseases.

RESULTS

Characterization of MNs

The fabrication process of the MN patches is shown schematically in fig. S1. The prototype MN-AAV patch was 6 mm in diameter and contained 44.75 ± 1.28 needle tips with base widths of 334 ± 22.88 μm, spacing of 465.3 ± 39.51 μm, and heights of 850 ± 3.25 μm as shown in the scanning electron microscopy (SEM) image (Fig. 2A). The representative stress-strain curves are shown in Fig. 2B (left). Uniaxial tensile tests showed that the MNs had a Young's modulus of 13.13 ± 1.34 MPa, while the MN-AAV had a Young's modulus of 12.28 ± 0.80 MPa. The Young's modulus of the MN group was higher than that of the MN-AAV group; however, this difference was not significant ($P > 0.05$) (Fig. 2B). Both the MN and MN-AAV had higher moduli than the native myocardium (modulus, several tens of kilopascal), indicating that the stiffness of the MNs with or without AAV loading was sufficient to penetrate the soft myocardium.

Swelling capacity

The swelling capacity of the MN bodies was monitored, and volume expansion was measured and calculated using a previously published method. The mean base diameter of the swollen MN bodies among three patches was 670.5 ± 81.63 μm, 678.9 ± 89.17 μm, and

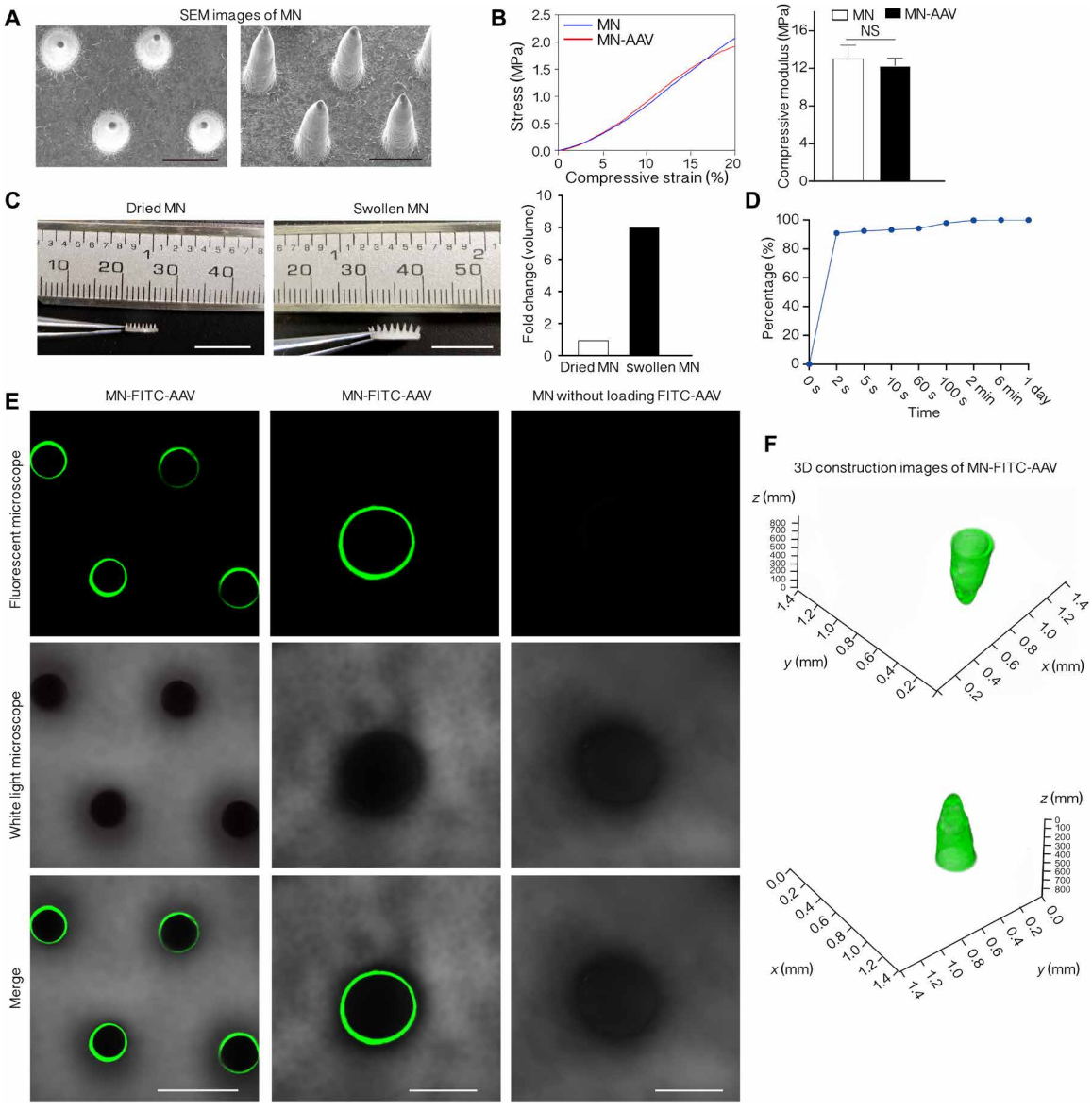

Fig. 2. Properties of MNs. (**A**) SEM images of MNs. (**B**) Representative stress-strain curves between the group of MNs with AAV (MN-AAV) or MNs without AAV. The histograms represent the comparison test of the two groups. $n = 4$ patches in each group. (**C**) Transitions between the dried and swollen states of the MNs. The histograms show the fold changes in MN volume between the dried and swollen stages ($n = 8$ MN tips, randomly selected from three patches). Photo credits: Hongpeng Shi, Department of Cardiac Surgery, Ruijin Hospital, Shanghai Jiao Tong University School of Medicine. (**D**) Release kinetics of MN-AAV. (**E**) Fluorescent images (scale bars, 500 μm) and magnified images (scale bars, 250 μm) indicating MNs surface-coated with FITC-AAV (green) particles and MNs without loading of FITC-AAV. (**F**) The three-dimensional (3D) construction images of MN-FITC-AAV. All data are reported as the means ± SD. NS, not significant.

683.4 ± 67.31 μm. The mean height of the swollen MN bodies was 1704 ± 56.75 μm, 1701 ± 73 μm, and 1705 ± 66.63 μm. Measurements of total recorded MN tips in height and base diameter were 1704 ± 64.89 μm and 677.6 ± 78.93 μm, respectively, which were significantly greater than those of the MN bodies in the initial state. The transitions between the dried and swollen states of MNs are shown in Fig. 2C. Swelling led to an 8.3-fold variation, indicating that the MN tips exhibited a high swelling ratio.

AAV release profile of MNs

Quantification of AAV release into supernatant collected after incubation at predetermined time points indicated a burst release model. A schematic of the experimental procedures performed to collect the released AAV fluid is provided in fig. S2. As shown in Fig. 2D, burst release led to increased initial AAV delivery, as follows: 90.93% of the virus was released in a 2-s period, while 92.42% of the virus was released in a 5-s period, and slower release followed the initial rapid release. Almost complete release was achieved by 24 hours. The titers of elution fluid released from MN-AAV ($n = 3$) were determined by real-time polymerase chain reaction (PCR), which indicated that 4.93×10^{10} vector genomes (vg) of AAV were loaded in each MN array. We also loaded greater amounts of AAV (the quantity of loaded AAV achieved 10^{11} vg) with three gradient quantities (1×, 1.5×, and 2×; $n = 4$ patches in each group). The amounts

of loaded AAV were calculated to be 3.14×10^{11} vg, 5.04×10^{11} vg, and 6.03×10^{11} vg, respectively; the fold differences of these groups were 1-, 1.69-, and 2.02-folds, respectively. Consequently, we could control the quantity of loaded vectors in each MN array by varying the amount of AAV solutions added. Furthermore, MNs exhibited outstanding drug-loading capacity.

Fluorescent labeling of AAV with FITC

To confirm AAV binding, we performed a critical examination of virus labeling with FITC dyes. As expected, compared with the control MNs without FITC-AAV, the AAV-loaded MNs revealed a strong fluorescence signal on the surface of the MN bodies (Fig. 2E, left and middle). Conversely, a specific fluorescence signal was absent in the control MN group (Fig. 2E, right). Ortho view (fig. S3) of a confocal laser scanning micrograph of *z*-stack images visualizes the MN tip as transverse section (*x*-*y*) and lateral section (*x*-*z* and *y*-*z*) views. The three-dimensional (3D) images generated by confocal microscopy confirmed that FITC-labeled AAV was successfully coated on the surface of the MN bodies (Fig. 2F). The fluorescence intensity of the fluorescent images acquired by confocal microscopy at the middle of MN bodies (400 μm from the base) was measured and compared among 11 randomly selected MNs in one patch. The average optical was measured using Image-Pro Plus software to evaluate the fluorescence intensity. The fluorescence intensity was 0.1127 ± 0.0233 with a little variation among the MNs. In addition, the intensity analysis at the middle of MN bodies among three MN patches (8 or 11 MNs were randomly selected from each patch) was measured and compared. No differences were observed among three patches (0.1127 ± 0.0233 versus 0.1156 ± 0.0254 versus 0.1084 ± 0.0279, all $P > 0.05$ in the multigroup comparisons) (fig. S4A).

Measurement of transgene expression in vitro

A schematic of the cell culture procedures is provided in Fig. 3A. The released vectors were tested for their infectious capacity and transgene expression in human embryonic kidney (HEK) 293 cells by flow cytometry and fluorescence microscopy. After a 3-day incubation, the distribution of GFP-positive cells was determined using fluorescence microscopy (Fig. 3B). Flow cytometry analysis revealed

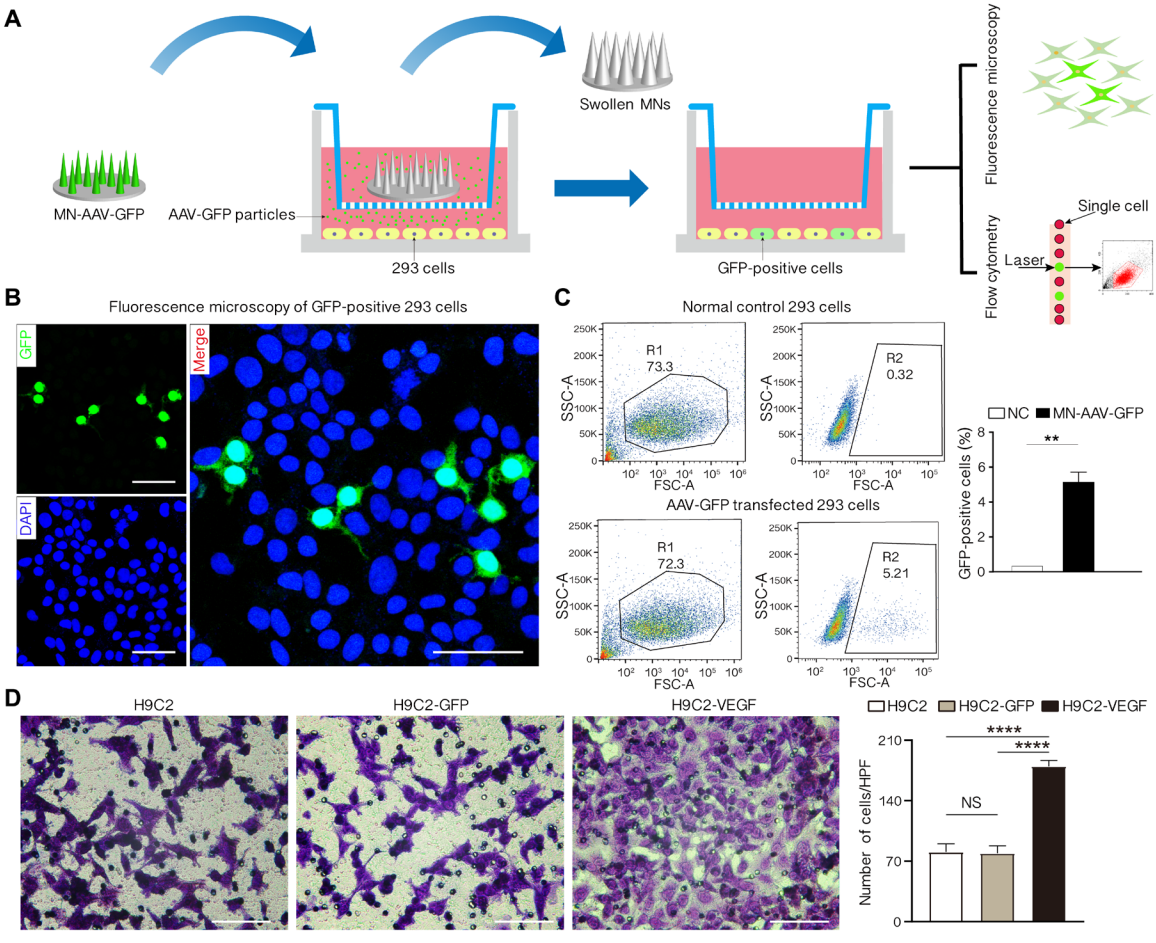

Fig. 3. Gene transfection and expression of MN-AAV in vitro. (**A**) Schematic of the cell culture experimental procedures performed to investigate the cell infectivity of released AAV. (**B**) Representative fluorescent images of GFP-positive cells in the MN-AAV-GFP group captured under a confocal microscope. Scale bars, 100 μm. DAPI, 4′,6-diamidino-2-phenylindole. (**C**) Qualification and comparison of GFP-positive cells between normal 293 cells and AAV-GFP transfected cells as detected by flow cytometry. SSC-A, side-scatter area; FSC-A, forward-scatter area. (**D**) Representative images of crystal violet–stained migratory human umbilical vein endothelial cells (HUVECs) on the porous membranes of Transwell inserts among the three groups and histograms of the numbers of migrated cells. Five random fields were selected for the statistical analysis. All data are reported as the means ± SD. $^{**}P < 0.01$ and $^{****}P < 0.0001$.

that 5.14% of the cells were transduced by the supernatant released from MN-AAV2-GFP (Fig. 3C). A comparison analysis of the GFP-positive cells indicated that the percentage of positive cells was significantly different between the MN-AAV2-GFP and normal control (NC) groups ($P = 0.0045$). We evaluated the efficiency of AAV9 transduction into HEK 293 cells between virus-containing MNs subjected to a freeze-thaw process (MN-AAV-FT) and those not subjected to a freeze-thaw process (MN-AAV-NFT). There was no difference between the MN-AAV-FT and MN-AAV-NFT groups (the relative percentage of the transduction efficiency was 97.2% versus 100%) (fig. S5).

Human umbilical vein endothelial cells migration assay

The angiogenic effect of AAV-VEGF was evaluated in vitro. Endothelial cell migration is of great importance in neovessel formation; therefore, the influence of the AAV-VEGF–transfected H9C2 cell culture supernatant on human umbilical vein endothelial cell (HUVEC) migration was assessed. The assay indirectly proved that the H9C2 cells infected by MN-AAV-VEGF released vectors could secrete VEGF into the culture supernatant, which strongly stimulated HUVEC migration [179.8 ± 6.76 per high-power field (HPF) in the H9C2-VEGF group] compared to that observed in the AAV-GFP–infected H9C2 cells (79.2 ± 8.53 per HPF in the H9C2-GFP group, $P < 0.0001$) and the NC H9C2 group (80.8 ± 9.34 per HPF, $P < 0.0001$; Fig. 3D).

Confirmation of MN insertion

Figure 4A briefly illustrates the procedures used to demonstrate successful AAV delivery and gene transfection mediated by MN-AAV in vivo. The precise region of the rat heart that received the methylene blue–loaded MNs was imaged and dissected. A customized vacuum apparatus was used for the implantation of MN patch (Fig. 1A and movies S1, S2, and S3). As shown in Fig. 4B and movies S3 and S4, the epicardium with puncture spots and the myocardium were stained by the released dyes. Similarly, MN- FITC-AAV were used to further confirm the successful insertion of the MNs. Fluorescent images of the horizontal and vertical sections of the LV wall indicated the penetration of the MNs, which resulted in an even distribution of agents (Fig. 4C, middle) compared to the distribution in the DI group (Fig. 4C, left). The fluorescence intensity in horizontal sections of rat hearts (Fig. 4C, middle) after MN-FITC-AAV administration ($n = 3$ animals; 15 puncture points were analyzed in each fluorescent image) was measured, and no significant differences were observed (0.1324 ± 0.0172 versus 0.1289 ± 0.0207 versus 0.1337 ± 0.0212, all $P > 0.05$ in the multigroup comparisons), confirming the uniformity of AAV loading (fig. S4B). In the transverse plane of the LV following MN-FITC-AAV application (Fig. 4C, right), the penetration depth of MNs into the LV wall was approximately 1000 μm.

Safety of MN application and gene delivery in vivo

Inflammatory staining was performed on sections from hearts subjected to MN-AAV and DI-AAV treatments to reveal signs of tissue inflammation. Normal rats were used as controls. We quantified CD68-positive inflammatory cell infiltration and found that the tissue densities of CD68-positive cells were indistinguishable among the three groups ($P > 0.05$) (fig. S6). In addition, we examined the heart performance of rats that underwent MN administration, which also confirmed the safety of the MN patch. The echocardiographic results indicated that MN application did not induce any functional impairment. Ejection fraction (EF), fractional shortening (FS), left ventricular systolic inner diameter (LVIDs), and left ventricular diastolic inner diameter (LVIDd) values were recorded and compared to those of normal rats (all $P > 0.05$) (Fig. 4D).

In vivo gene transfer and bioluminescence imaging

To trace the expression of luciferase delivered by MN-AAV-LUC in living animals 4 weeks after MN-AAV administration, we applied a noninvasive small animal bioluminescence imaging system with high sensitivity. As shown in Fig. 4E (top), the AAV-LUC vectors transfected the target myocardium, resulting in high levels of luciferase expression in the heart, while no bioluminescence signals were detected in NC rats. In addition, proteins were extracted from the MN-AAV-LUC and NC groups, and an antifirefly luciferase antibody was used to detect the expression in Western blot (WB) assays (Fig. 4E, bottom), which indicated successful AAV delivery into and transfection of the myocardium.

GFP expression and distribution

To characterize the distribution of gene expression mediated by MN patches or DI, we analyzed rats that were subjected to gene delivery with AAV vectors encoding a GFP reporter gene. GFP-positive cells were detected in the anterior wall of the LV. The distribution of gene expression following the MN application was marked by an almost even distribution (Fig. 4F, top). In contrast, in the DI group, as described in previously published studies, the transfected cardiomyocytes were mainly confined to the site of the injection (Fig. 4F, middle). The distribution of fluorescent signals at five randomly selected horizontal lines in the fluorescent images was measured by ImageJ software (ImageJ 1.47v, National Institutes of Health). The results were plotted and fitted with OriginPro 8.5 software (OriginLab Corp., Northampton, MA, USA). The fluorescent signals were scattered evenly in the MN-AAV-GFP group, while in the DI-AAV-GFP group, the signals were confined to a specific region (Fig. 4F, bottom). The merged images of the two groups vividly demonstrated the variation in the distributions. No GFP-positive cells were found in the organs of lungs, kidneys, liver, or skeletal muscles, as shown in fig. S7. As indicated by representative in vivo images, no luciferase signals were observed in the defined organs, as shown in Fig. 4E (top).

MN-VEGF ameliorated cardiac dysfunction in MI rats

To assess variations in cardiac function, we measured EF, FS, LVIDs, and LVIDd by echocardiography 2 days after left anterior descending coronary artery (LAD) ligation (baseline data) and 4 weeks after MN application (end point data). The study design for the AAV-VEGF treatment via MNs is illustrated in Fig. 5A. The parameters of the four groups (the MI, MI + MN, MI + DI-VEGF, and MI + MN-VEGF groups) measured at baseline did not differ significantly, indicating equivalent heart performance (fig. S8). Twenty-eight days after MN application, the rats with MI that received MN-VEGF had the greatest EF and FS values and the smallest LVIDs and LVIDd values (Fig. 5B and fig. S9A). EF was improved in the MN-AAV-VEGF group compared with the DI-AAV-VEGF (36.10 ± 5.25% versus 30.29 ± 2.10%, $P = 0.042$), MI (36.10 ± 5.25% versus 24.28 ± 4.34%, $P = 0.0003$), and MI + MN (36.10 ± 5.25% versus 24.03 ± 5.87%, $P = 0.0002$) groups. The MI + MN-VEGF group showed greater FS (18.28 ± 2.97%) than the DI-AAV-VEGF group (15.04 ± 1.05%, $P = 0.0034$), the MI + MN group (11.76 ± 3.05%, $P = 0.0002$), and the MI group (11.93 ± 2.27%, $P = 0.0002$). LVIDd and LVIDs in the MN-AAV-VEGF group were significantly lower than those in the

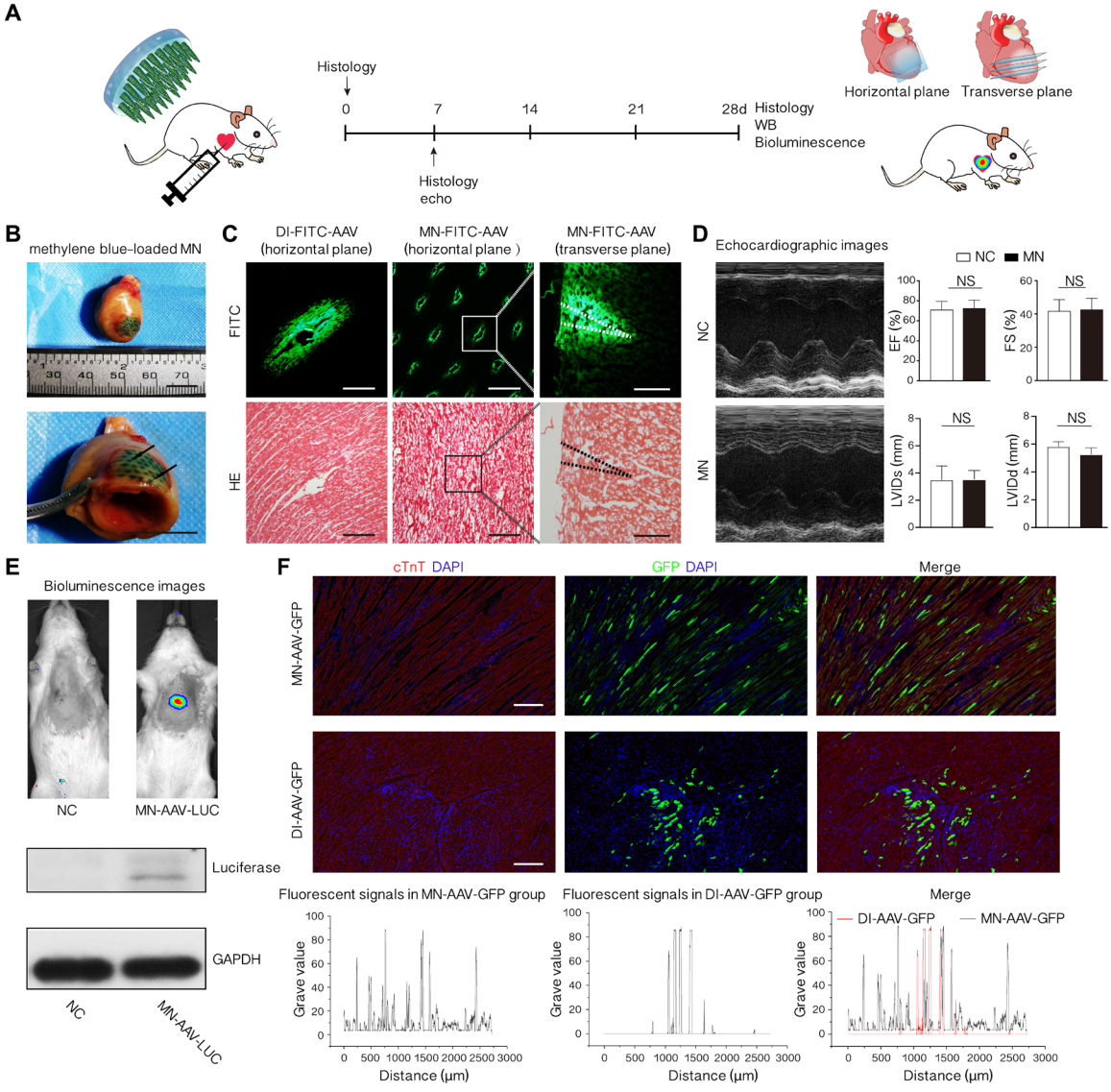

Fig. 4. Successful AAV delivery and gene transfection of MN-AAV in vivo. (**A**) Schematic illustrating the study design, involving the MN application in this section. (**B**) Confirmed insertion of methylene blue–loaded MNs into the myocardium. The black arrow denotes an area of methylene blue–stained myocardium. Photo credits: Hongpeng Shi, Department of Cardiac Surgery, Ruijin Hospital, Shanghai Jiao Tong University School of Medicine. (**C**) Representative fluorescent and hematoxylin and eosin (HE) images of LV walls that received DI of FITC-AAV and MN-FITC-AAV. The LV wall was cryosectioned horizontally ($n = 3$ animals per group; scale bars, 500 μm) or transversely (scale bars, 400 μm) for the MN-FITC-AAV–treated hearts. The dashed line denotes the shape of MN-FITC-AAV following application. (**D**) Representative echocardiographic images and left ventricular function parameters between the MN and NC groups. The data are presented as the means ± SD; $n = 3$ animals per group. (**E**) Representative images of bioluminescence ($n = 5$ animals per group) and Western blot (WB) assay results ($n = 3$ animals per group) 4 weeks following MN application. GAPDH, glyceraldehyde-3-phosphate dehydrogenase. (**F**) Representative fluorescence micrographs showing the spatial distribution of GFP-positive cells (green) in the MN-AAV-GFP and DI-AAV-GFP groups at day 28. Cardiomyocytes were identified by anti-cTnT (cardiac troponin T) antibodies (red); nuclei were stained with DAPI (blue). $n = 5$ animals per group. Scale bars, 200 μm. Separated and merged distribution data of fluorescent signals between the MN-AAV-GFP and DI-AAV-GFP groups are presented. All data are reported as the means ± SD.

MI group (LVIDd, 9.12 ± 1.09 mm versus 10.55 ± 0.69 mm, $P = 0.0179$; LVIDs, 7.59 ± 1.01 mm versus 9.33 ± 0.81 mm, $P = 0.0048$). The absolute changes in heart function (ΔEF and ΔFS) are shown in Fig. 5B. The MI and MI + MN groups showed significantly worse cardiac function in terms of the two parameters than the DI-AAV-VEGF and MI + MN-VEGF groups (ΔEF, −18.77 ± 2.36% in the MI group versus −6.07 ± 4.63% in the MI + MN-VEGF group, $P < 0.0001$; ΔFS, −9.97 ± 1.25% in the MI group versus −3.14 ± 2.48% in the MI + MN-VEGF group, $P < 0.0001$). Compared with the DI-AAV-VEGF, MI, and MI + MN groups, the MN-AAV-VEGF group showed a lack of significant change in cardiac function. Thus, MN-mediated VEGF expression improved cardiac function.

MN-VEGF reduced infarcted areas and improved adverse remodeling

The infarction size and scar area were measured according to our previously described methods (*26*). Masson's trichrome staining and magnified images revealed the morphology and fibrosis of heart tissues

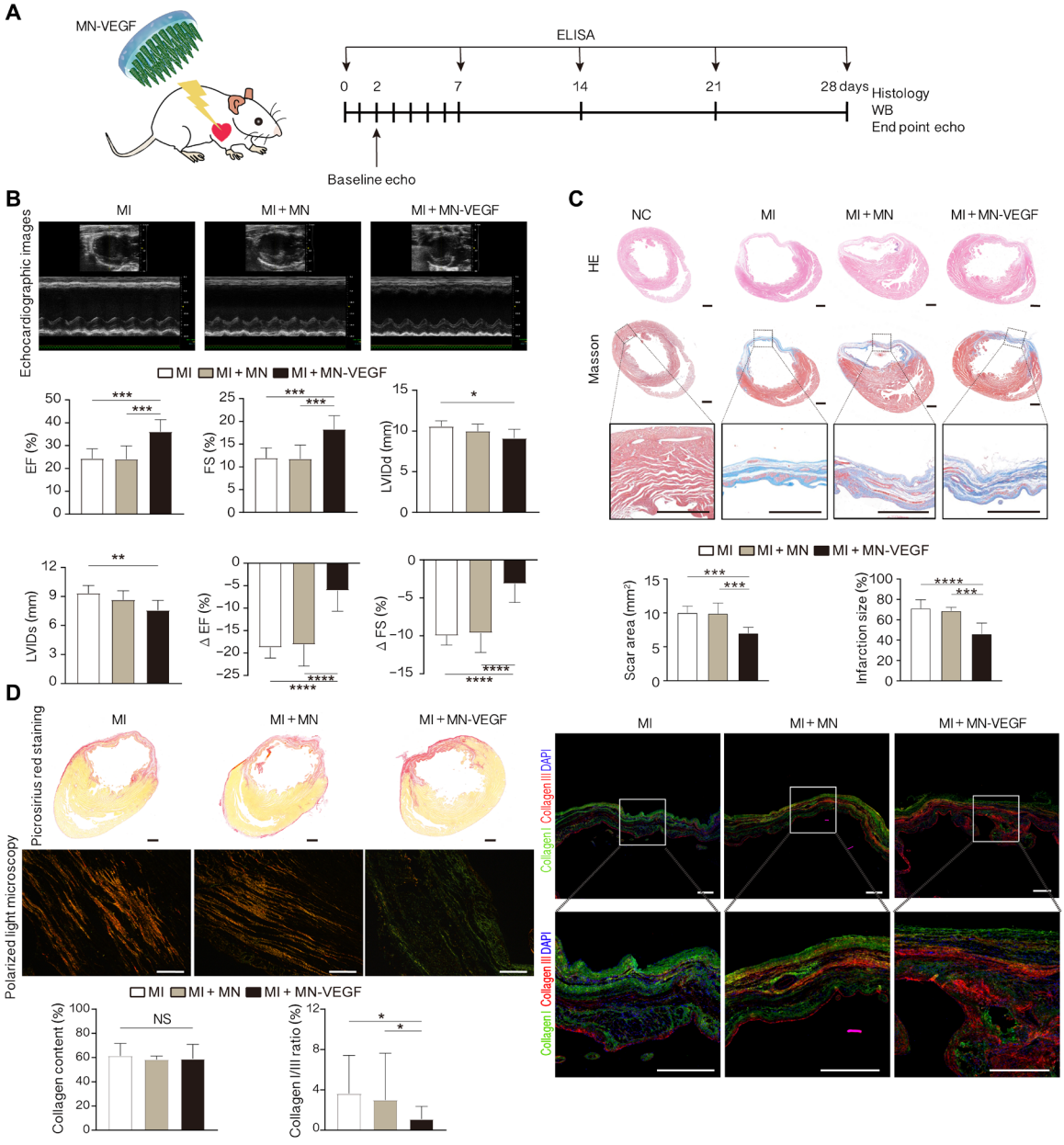

Fig. 5. AAV-VEGF ameliorated cardiac dysfunction. (**A**) Schematic illustrating the study design involving MN-AAV-VEGF application and improvement of injured heart function. (**B**) Representative echocardiographic images of the experimental groups 4 weeks following MN application. Left ventricular function parameters (EF, FS, LVIDs, and LVIDd) and absolute changes in heart function (ΔEF and ΔFS) were also measured and compared among the three groups. $n = 6$ animals per group. (**C**) Representative Masson's trichrome–stained myocardial sections 4 weeks after MN-AAV-VEGF application. The scar areas and infarct sizes were quantified on the basis of Masson's trichrome–stained images. Scale bars, 1 mm. (**D**) Identification of collagens via picrosirius red staining among the three groups. Scale bars, 1 mm. Representative polarized light images of the picrosirius red–stained sections were subjected to polarized light microscopy. Scale bars, 100 μm. Histograms showing the comparisons of collagen content and the type I/type III collagen ratios among the three groups. Right: Representative fluorescence micrographs identifying type I collagen (green) and type III collagen (red); the nuclei were stained with DAPI (blue). $n = 3$ animals per group. Scale bars, 500 μm. All data are reported as the means ± SD. *$P < 0.05$, **$P < 0.01$, ***$P < 0.001$, and ****$P < 0.0001$.

(Fig. 5C and fig. S9B). Compared to those in the MI and MI + MN groups (10.04 ± 0.94 mm^2 and 9.92 ± 1.54 mm^2, respectively), the scar areas (Fig. 5C, bottom) in the MI + MN-VEGF group (7.02 ± 0.85 mm^2) and the MI + DI-VEGF group (8.47 ± 0.82 mm^2) were effectively controlled by MN-VEGF application (fig. S9B). There were significant differences between the MI + MN-VEGF group and the control group (MI + MN-VEGF versus MI, $P = 0.0004$; MI + MN-VEGF versus MI + MN, $P = 0.0006$; MI + MN-VEGF versus MI + DI-VEGF, $P = 0.049$). In addition, the infarct size (Fig. 5C, bottom) was not different between the MI (71.27 ± 8.37%) and MI + MN (68.86 ± 3.25%) groups ($P = 0.6187$). The infarct size was reduced in the AAV-VEGF–treated groups (56.48 ± 5.64% in the

MI + DI-VEGF group and 46.17 ± 10.68% in the MI + MN-VEGF group) ($P < 0.0001$ in the MI + MN-VEGF group compared with the MI group, $P = 0.0002$ in the MI + MN-VEGF group compared with the MI + MN group, and $P = 0.00458$ in the MI + MN-VEGF group compared with the MI + DI-VEGF group).

Picrosirius red staining combined with polarization microscopy was used to examine collagen fibers and to quantitatively determine their levels and types in scars in the four groups (Fig. 5D, left, and fig. S9C). Type I collagen was identified by yellow or red staining, and type III collagen was indicated by green staining under polarized light. The total collagen content in the infarcted region was similar among the groups, indicating no difference in collagen deposition (61.42 ± 10.24% in the MI group, 58.97 ± 11.83% in the MI + MN group, 60.16 ± 3.86% in the MI + DI-VEGF group, and 58.97 ± 11.83% in MI + MN-VEGF group, all $P > 0.05$). Moreover, the ratio of type I to type III collagen (type I/type III) was increased in the MI and MI + MN groups (3.63 ± 3.79% versus 2.99 ± 4.64%, $P > 0.05$). However, the ratio in the MI + MN-VEGF group (1.11 ± 1.24%) was lower than those in the MI and MI + MN groups ($P < 0.05$). The ratio in the MI + DI-VEGF group (1.89 ± 1.44%) was slightly higher than that in the MI + MN-VEGF group; however, this difference was not statistically significant ($P = 0.2254$). In addition, costaining of sections with type I (green) and type III (red) collagen antibodies was used for visualization of the collagen types (Fig. 5D, right, and fig. S9C).

Functional neovascularization by MN-VEGF

To investigate the angiogenic and arteriogenic effects of MN-VEGF in the border zone and infarction region, we used antibodies against von Willebrand factor (vWF) and α-smooth muscle actin (αSMA) to stain endothelial cells and vascular smooth muscle cells, respectively. Tubular structures stained by fluorescent antibodies were identified as vessels. The capillary density was estimated on the basis of the vWF-positive vessels per HPF, and the arterial density was evaluated on the basis of αSMA-positive vessels per HPF using the data collected at 4 weeks. The mature index was quantified as the ratio of αSMA-positive vessels to the total number of vessels (*27*). As illustrated in Fig. 6B and fig. S9D, in the infarction region, the capillary density in the MI group was identical to that in the MI + MN group (8.33 ± 1.51 per HPF versus 8.33 ± 1.97 per HPF, $P > 0.05$). However, the value in the MI + MN-VEGF group (39.67 ± 11.15 per HPF) significantly differed from that in the MI ($P < 0.0001$), MI + MN ($P < 0.0001$), and MI + DI-VEGF (25.83 ± 5.19 per HPF, $P = 0.0011$) groups. Regarding the capillary density in the border zone, no difference was found between the MI and MI + MN groups (14.17 ± 1.72 per HPF in the MI group and 14.17 ± 2.40 per HPF in the MI + MN group, $P > 0.05$). The capillary density in the MI + MN-VEGF group was 72.67 ± 13.46 per HPF ($P < 0.0001$ compared to those in the MI and MI + MN groups and $P = 0.0002$ compared to that in the MI + DI-VEGF group). The arterial density was compared as shown in Fig. 6B and fig. S9D. Compared to the MI + MN-VEGF group (38.83 ± 9.77 per HPF, all $P < 0.0001$), the MI and MI + MN groups (3.83 ± 1.72 per HPF in the MI group and 3.67 ± 1.03 per HPF in the MI + MN group, $P > 0.05$) showed decreases of ~90% in the infarction region. In addition, the arterial density of the MI + MN-VEGF group was significantly higher than that of the MI + DI-VEGF group (24.50 ± 4.85 per HPF, $P = 0.0012$). In the border region, the arterial density was 6.67 ± 2.50 per HPF in the MI group and 7.17 ± 2.23 per HPF in the MI + MN group ($P > 0.05$). In the MI + MN-VEGF group, the arterial density was 66.83 ± 12.86 per HPF ($P < 0.0001$ compared to those in the MI and MI + MN groups and $P = 0.0025$ compared to that the MI + DI-VEGF group). As shown in Fig. 6B and fig. S9D, the mature index in the infarction region was 36.55 ± 11.60% in the MI group and 37.40 ± 10.53% in the MI + MN group, with no difference between the two groups. In the MI + MN-VEGF group, the value was 86.3 ± 1.67%, which was better than that in the MI ($P < 0.0001$), MI + MN ($P < 0.0001$), and MI + DI-VEGF (83.88 ± 5.41%, $P > 0.05$) groups. No significant difference in the mature index was observed between the MI + MN-VEGF (85.20 ± 4.46%) and MI + DI-VEGF (84.53 ± 6.24%, $P > 0.05$) groups. The mature index in the MI + MN-VEGF group was markedly greater than that in the MI (39.97 ± 13.85%) and MI + MN (41.73 ± 9.23%) groups (all $P < 0.0001$). No significant differences in serum VEGF levels were detected at various time points between the MN-VEGF and MI groups (all $P > 0.05$) (Fig. 6C). The samples were measured in duplicate.

Signaling pathways activated by MN-VEGF

The binding of VEGF to VEGF receptor 2 (VEGFR2) leads to the activation of diverse intracellular extracellular signaling pathways. WB analysis (Fig. 6D) showed that VEGF and VEGFR2, the high-affinity receptor of VEGF, were significantly up-regulated (all $P < 0.05$). The Akt and phosporylated Akt protein levels in AAV-treated hearts were significantly higher than those in non-AAV–treated MI hearts (all $P < 0.05$). The protein level of phosphoinositide 3-kinase (PI3K) in the MI + MN-VEGF group was increased, although the difference was not significant ($P > 0.05$). The level of the proapoptotic protein caspase 9 was significantly decreased in the MI + MN-VEGF group ($P < 0.05$).

DISCUSSION

CVD is the primary cause of mortality worldwide (*28*). Intramyocardial injection of therapeutic agents is a treatment strategy for patients suffering from this disease (*29*). Although local injection is a commonly used administration method to deliver agents to the myocardium, the effects are inevitably restricted to the injection site (*9*–*11*), which is attributed to the localized high concentrations of the agents. In addition, unlike in other organs, the injected agents can be extruded from the myocardium due to continuous dynamic muscle contraction. As reported in the published literature, a primary obstacle to cell therapy is the extremely low rate of myocardial retention after intramyocardial injection (*13*). It has been reported that almost 5 to 15% of intramyocardially injected cells are retained within the myocardium (*30*, *31*); thus, only a fraction of injected cells contribute to therapeutic benefit. Development of new types of instruments and technologies to overcome this disadvantage is desperately needed. Figure S10 represents our vision for the clinical translation of MNs, in which MNs will be used to deliver therapeutic agents via a small thoracic incision to decrease the risk of infection induced by open-heart surgical procedures. Different from traditional approach of gene delivery, we developed an MN-AAV to deliver target gene into the myocardium. Coronary artery revascularization [percutaneous coronary intervention (PCI) or coronary-artery bypass grafting (CABG)] is an established therapeutic intervention. However, myocardial revascularization for ischemic regions with small coronary arteries remains a challenge in clinical practice. Gene therapy to improve vascular perfusion of those ischemic regions might be a promising alternative choice, especially for patients with IHD who

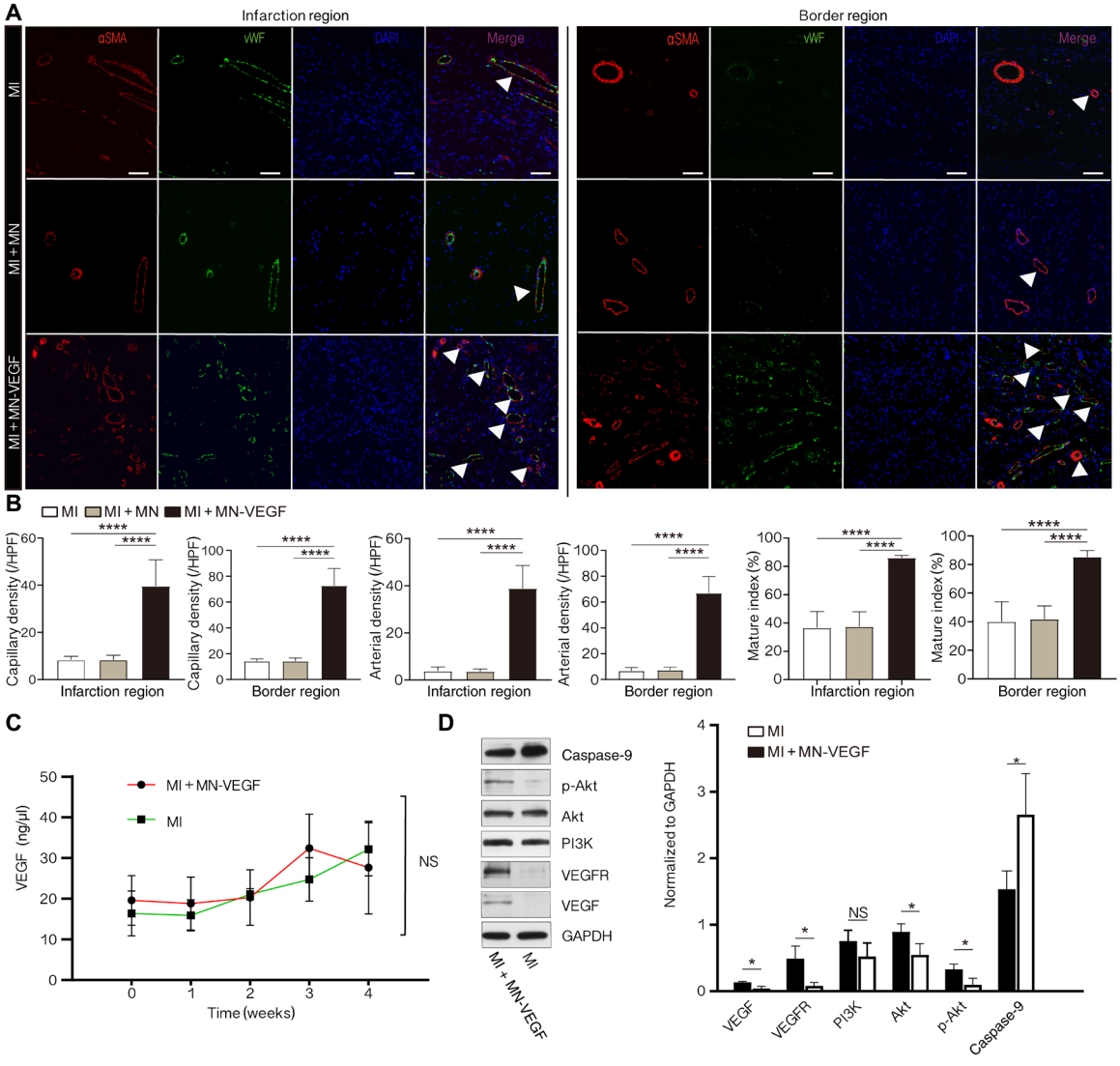

Fig. 6. Neovascularization and activation of signals by MN-AAV-VEGF. (**A**) Representative immunofluorescent images of vWF (green) and αSMA (red) in the tissues of the infarction and border region showing increased vessel density in the MN-AAV-VEGF group compared with those in the other two groups. $n = 3$ animals per group. Scale bars, 50 μm. Vessels are indicated by white triangles. (**B**) Quantification of capillary density, arterial density, and the mature index among the three groups in the infarction and border regions. (**C**) VEGF levels were detected by enzyme-linked immunosorbent assay (ELISA) in serum from the MI + MN-VEGF and MI groups. $n = 3$ animals per group. (**D**) Representative WB results for VEGF, VEGF receptor (VEGFR), phosphoinositide 3-kinase (PI3K), Akt, phosphorylated Akt (p-Akt), and caspase-9 in heart homogenates from the MI + MN-VEGF and MI groups. $n = 3$ animals per group. The bar graphs show the quantified protein levels. All data are reported as the means ± SD. *$P < 0.05$ and ****$P < 0.0001$.

are not candidates for PCI or CABG. In addition, because of the poor gene transfer efficiency in the myocardium and the inability of the therapy to target ischemic myocardium, the transduction efficiency was reduced. Thus, delivering MNs via less invasive surgeries repeatedly might improve the efficiency of gene transfection.

Angiogenic gene therapy for IHD is a promising option for the treatment of MI (*32*, *33*). VEGF is important for the development and differentiation of the vascular network, with favorable preclinical evidence showing that it notably increases perfusion, improves tissue metabolism, improves cardiac function, and provides cardiac protection. However, intracoronary administration of VEGF protein has not yielded much clinical success (*34*). The principal limitation of administration of this protein is the short half-life of exogenous proteins in target tissue, which reduces the therapeutic benefit (*35*). To prolong the effects of angiogenic cytokines, recombinant plasmid DNA and viral vectors can be used, which allow for the consistent replication of the VEGF gene and maintain long-lasting protein expression in transfected cells. A series of studies have demonstrated improvement in rodent and large-animal (dog, sheep, and pig) models of ischemia and infarction following gene therapy with VEGF (*36*–*38*). Similar results were obtained in our study. MN-AAV-VEGF ameliorated cardiac dysfunction in a rat model of MI. Therefore, the application of proangiogenic substances may be a new treatment option for patients with IHD. However, the results have not been very promising except for safety; follow-up conducted for over 10 years has indicated that there are no significant transgene or vector-related side effects (*39*).

On the other hand, previously published research has reported that high levels of circulating VEGF in acute MI can induce acute cor pulmonale, resulting in increased mortality (*40*). Unregulated and continuous expression of VEGF has been reported to lead to angioma formation at the site of injection (*33*, *41*). However, in the future, cardiomyocyte-targeted viruses and improved gene transfection efficiency may enable the delivery of AAV vectors at low starting doses through repeated administration to control the expression of angiogenic factors. Furthermore, the side effects caused by VEGF overexpression might be ameliorated by regulation of gene expression, such as through gene switching, and other therapeutic approaches, such as antiangiogenic therapy using anti-VEGF antibodies. The management of angiogenic factor expression in both serum and target regions is important for enhancing the local therapeutic efficiency of this method and decreasing possible adverse effects (*32*). Consequently, careful application-specific consideration is warranted when selecting a processing strategy that minimizes unwanted responses.

To overcome difficult obstacles associated with the DI mode of agent administration, we fabricated MN-AAV to deliver the VEGF gene to rat hearts, which led to optimal distribution and local therapeutic efficiency. In addition, the coated vectors instantly penetrated into the myocardium, thus improving the retention of the delivered drugs, which indicated a better therapeutic effect in the MI + MN-VEGF–treated group than in the MI + DI-VEGF group. No significant differences in VEGF levels were detected at various time points between the MI + MN-VEGF and MI groups (Fig. 6C), similar to the results of experiments using large-animal models (*32*). In addition, no GFP or luciferase expression was detected in other organs (fig. S7 and Fig. 4E).

Versatile MN patches were fabricated according to our previously reported method (*20*) and were eventually machined into the desired sizes to achieve various characteristics, including sufficient strength to penetrate the target myocardium (Fig. 4B), water-swelling capacity (Fig. 2C), high drug-loading capacity, drug-loading uniformity (fig. S4), and therapeutic burst release kinetics (Fig. 2D). The phase transition capability allows efficient drug diffusion from a drug reservoir through a polymeric matrix with predictable accuracy (*42*). Researchers have long sought to control and overcome the burst release of agents during the application of MNs (*43*). However, this shortcoming was effectively used to deliver agents to the myocardium in this study. The intrinsic properties of the MNs and the modified AAV harboring approach resulted in a unique kinetic profile characterized by enhanced AAV delivery with predictable accuracy and early burst release kinetics. Extended release behavior in vitro was detected and confirmed by the AAV tilter assay (Fig. 2D). Combined with in vivo studies (Figs. 5 and 6), AAV-VEGF–loaded MN can effectively ameliorate cardiac functions, reduce the scar size, and elevate myocardial perfusion in rat MI model, which suggested that MN-mediated gene delivery to targeted heart regions. Considering that we developed an MN-AAV to deliver gene vectors to repair injured myocardium and the isolated rat heart will suffer various pathophysiologic alterations after being removed from the living body, it is hard to simulate the complicated situations in the body by using Franz diffusion cells. Consequently, the release experiment by using Franz diffusion cell involved heart tissue is not conducted in our study. In addition, researchers have reported that the drug release results obtained using phosphate-buffered saline (PBS) and Franz diffusion cell were comparable (*44*–*46*), indicating that these two experiments may be equivalent in representing the release profile of MNs. Regarding AAV loading, specific fluorescence imaging was absent in the control MNs, conversely, the surfaces of the` MN-FITC-AAV revealed a strong fluorescence signals (Fig. 2E), and the fluorescence intensity of MNs was identical among different patches, indicating the uniformity of drug loading in the MNs. In addition, the 3D images constructed by confocal microscopy confirmed that FITC-AAV was successfully and uniformly coated onto the surfaces of the MN bodies (Fig. 2F).

Hematoxylin and eosin (HE) staining of sections from hearts subjected to MN treatment revealed no signs of tissue necrosis, as shown in the representative sections. Although the wound area was relatively larger, the pinhole produced by each MN was quite small, and the tissue around each pinhole was not damaged (Fig. 4C). These results demonstrated that the wounds on the hearts might be acceptable and might self-heal after a period of time. Whether application in the hearts of large animals will result in any damage needs to be further studied. The inflammatory staining of the heart sections and the unaffected performance of the hearts treated with the MNs further confirmed the safe application of MNs (Fig. 4D and fig. S6). Previous research has suggested that MNs serve as channels connecting the patch and the host myocardium. For example, MN-loaded cardiac stem/stromal cells can secrete paracrine elements to treat injured hearts with good biocompatibility in rats (*2*). The spatial distribution of gene transfer mediated by MNs was also evaluated in this study. GFP-positive cells were detected and well distributed in the anterior wall of the LV after MN treatment (Fig. 4F, top). In contrast, in the DI group (Fig. 4F, middle), as described in previously published studies, the transfected cardiomyocytes were confined to the site of the injection (*9*, *10*). MNs mediated gene delivery to the myocardium with a fine distribution and strong targeting precision. Analysis of MN-FITC-AAV– and methylene blue–stained MNs further confirmed the successful delivery of the released dyes and AAV particles into the myocardium with a homogeneous distribution (Fig. 4, B and C, and movies S3 and S4). The composite image of the in vivo imaging results also confirmed the targeted delivery of and transfection with the AAV-LUC vectors (Fig. 4E).

Given the safety and good distribution of MNs, we investigated the practicability of MN-mediated delivery of therapeutic agents, namely, AAV-VEGF, to the myocardium to treat injured hearts. First, the angiogenic effect of AAV-VEGF was tested in vitro. The HUVEC migration assay indicated that the culture medium of VEGF-transfected H9C2 cells had a powerful influence on the migration of HUVECs (Fig. 3D). The stimulation is an important step in neovessel formation (*47*). Then, MN-VEGF was used to treat the injured hearts. The echocardiographic results revealed significantly higher EF and FS values and significantly lower LVIDs and LVIDd values in the MN-VEGF group than in the DI-VEGF group and the other two control groups (Fig. 5B and fig. S9A), indicating functional improvement. No significant differences were observed in cardiac function between the MI and MI + MN groups. Significant decreases in the scar area and infarct size were observed in the MI + MN-VEGF–treated group, which showed outcomes superior to those in the three control groups (Fig. 5C). The increased expression of type I and type III collagen in infarcted zones has been suggested to protect hearts from remodeling and dilation (*48*). Although the differences among the four groups in total collagen content were not statistically significant, the ratio of type I to type

III collagen was greater in the control groups than in the MI + MN-VEGF–treated group (Fig. 5D and fig. S9C), showing that the application of MN-VEGF modified the composition of collagen in the infarct scars (predominantly favoring type III collagen). Type III collagen confers elasticity and increases compliance (*48*), which might lead to the improvement of heart function.

Several studies have reported that VEGF expression improves cardiac function through the induction of angiogenesis (*32*, *49*). Similar results were obtained in our study. As illustrated in Fig. 6A, compared with those in the control groups, the capillary and arterial densities in the scar tissue and border region were significantly increased in the MI + MN-VEGF group, which exhibited an elevated mature index. As previously reported, various signaling pathways, including the PI3K/Akt kinase pathway, were activated by the binding of VEGF to VEGFR, which can preserve cardiac performance (*50*). Consistent with the results from WB analysis of heart homogenates, the levels of many prosurvival proteins and a few proapoptotic proteins significantly differed in MI + MN-VEGF–treated hearts compared to MI hearts at 4 weeks after MN-VEGF application, indicating that signal transduction pathways were activated by the overexpression of VEGF (Fig. 6D).

This study has several limitations. First, the therapeutic effects of MN-VEGF were evaluated for 4 weeks in this study. In the future, longer time points should be used to determine the roles of MN-VEGF in regulating cardiac function. Second, to further broaden the clinical application of MNs, in vivo studies with large-animal models incorporating MN administration via minimally invasive surgery should be investigated.

In summary, we developed an AAV-loaded MN patch and showed that transepicardial permeation resulted in a homogeneous distribution of agents against direct local intramyocardial injection (after which the agents were confined to the site of injection). Our present study supports the practicality, safety, and versatility of MNs for delivery of therapeutic agents via minimally invasive surgery. This is a proof of concept study supporting translation to clinical applications.

MATERIALS AND METHODS

Fabrication and characterization of MNs

The MNs were prepared according to our previously described method (*20*). These MNs are made of polyvinyl alcohol (PVA) and are not degradable. They will swell and dissolve after 6 months. The PVA can form microcrystalline domains as cross-linking junctions to produce a PTM patch. The PTM achieves highly efficient delivery of drugs and carriers without depositing the needle tip materials into the body. Briefly, patches were prepared with an air-permeable but water-impermeable mold. A vacuum was applied to the back to suck the aqueous PVA solutions into the holes within the mold. Then, a freeze-thaw process was conducted to form microcrystalline domains to enhance the mechanical strength of the MNs. Drying and punching processes were used after detaching the MNs from the molds (fig. S1). The mechanical properties of the MNs with or without AAV loading were assessed by a universal testing machine (MTS Echo, Exceed 40, USA) equipped with Test Suite TW software and a 100-N loading cell (*51*). In the compression assay, every patch was compressed to a strain of 20% at a rate of 10 mm/min with an initial load of 0.01 N. The compressive modulus was automatic calculated according to the GB/T 1041-2008/B/0 standard in the machine program. The differential strain ($\varepsilon 2 - \varepsilon 1$) was 0.0025. A series of modulus was calculated at each point with strain of 0 to 20% and then was linearly fitted to obtain compressive modulus ($n = 4$ patches in each group). For testing and comparison of the swelling capability of the MNs, MN patches were immersed in PBS and incubated at 37°C for at least 1 day until completely swelled; then, the MNs were photographed and measured. At least three measurements were taken, and mean values were reported. The fold change in the tip volume, which was based on the presumption of a conical shape, was calculated to reveal the phase-transition capability of MNs (*52*).

Coating of AAV on the surfaces of the MN bodies

MN patches of the desired size (6 mm in diameter) were obtained with a punch. The patches were pierced through enlarged Parafilm (Parafilm M laboratory film) membranes (*53*). AAV9 vectors with cytomegalovirus (CMV) promoters containing the gene sequence for VEGF165 (AAV-VEGF) or GFP (AAV-GFP) alone were constructed by Shanghai GeneChem Co. Ltd. (Shanghai, China). An AAV9 vector with a CMV promoter containing the gene sequence for LUC (AAV-LUC) and an AAV2 vector with a CMV promoter containing the gene sequence for GFP (AAV2-GFP, which was used to assess the efficiency of transgene expression in vitro) were constructed by Hanbio (Shanghai, China). The AAV-containing solutions (~5×10^{10} vg) were dispensed to the patches and absorbed by the MN bodies. After completely drying in a customized low-temperature dryer, the film was peeled. The MN-AAV was used in in vitro and in vivo studies.

Fluorescent labeling of AAV

AAV was labeled with FITC (Thermo Fisher Scientific) according to a labeling protocol and a published paper (*54*). A Slide-A-Lyzer dialysis cassette (Slide-A-Lyzer Dialysis Cassette Kit, Invitrogen; 3.5K molecular weight cutoff, 3 ml) was applied to separate the unconjugated dyes. The yield of FITC conjugate was coated and immobilized onto the surfaces of the MNs with the aid of the intrinsic absorption capacity conferred by the phase-transition characterization.

AAV release profile

MN patches were affixed to the inner caps of 1.5-ml Eppendorf microcentrifuge tubes filled with PBS. The tubes were inverted and incubated in a thermostatic shaker (37°C with shaking at 100 rpm). The elution fluid was centrifuged to draw the solution from the cap to the base of the tube at 300*g* and collected at 2 s, 5 s, 10 s, 60 s, 100 s, 2 min, 6 min, and 1 day. Equal quantities of AAV were also detected as NCs. A scheme of these procedures is provided in fig. S2. In the published literature, real-time PCR has been applied to determine AAV titers (*55*). A real-time PCR assay of serial dilutions of plasmid vector standards and collected samples was performed in a Roche LC96 machine. The samples were preincubated at 95°C for 3 min and then subjected to 40 cycles of 94°C for 30 s (denaturation), 62°C for 30 s (annealing), and 72°C for 30 sec (amplification). The data were recorded as cycle threshold (C_t) values. C_t values are linearly correlated with the copy numbers of the templates in the exponential phase (*55*). The formula of the standard curve between the C_t value and the viral genome copy number was acquired from the standard samples. The titers of the released vectors in the samples were calculated according to the formula. The cumulative percentages of released vectors at different time intervals were calculated by dividing the values of the AAV quantity in the control group. The detection of each sample was performed in triplicate. In addition, the assay

was repeated three independent experiments, and the mean values of each time point were used for graph plotting (Fig. 2D).

Efficiency of transgene expression in vitro

HEK 293 cells were cultured in Dulbecco's modified Eagle's medium (Gibco, 11965092) supplemented with 10% fetal bovine serum (Gibco, 10270-106) and 1× penicillin-streptomycin (Gibco, 15070-063). Subconfluent 293 cells were seeded on the bottoms of the wells (Transwell culture inserts, pore size of 8 μm; Corning, 3422). Virus-containing MNs (n = 3, each MN patch contained ~5×10^{10} vg AAV2-GFP) were placed on the filter inserts and incubated in medium for 1 hour (Fig. 3A). The percentages of 293 cells transfected by the released AAV2-GFP vectors were determined by flow cytometry of 10,000 cells (Beckman Coulter). In addition, mounted 293 cells grown on cleaned coverslips in cell culture dishes were imaged using fluorescence microscopy. We evaluated the transduction efficiency of MN-AAV before and after the freeze-thaw process. Subconfluent 293 cells were seeded on the bottoms of the wells. Virus-containing MNs (subjected and not subjected to the freeze-thaw process; n = 5 in each group) were placed on the filter inserts. After a 3-day incubation, the percentages of GFP-positive cells were determined by flow cytometry.

Migration assays for HUVECs treated with AAV-VEGF–transfected cell culture supernatants

The culture supernatants of H9C2-VEGF cells transfected with released AAV-VEGF vectors and control groups (NC H9C2 cells and AAV-GFP transfected H9C2 cells) were collected. For migration assays, HUVECs (1×10^5 cells) in 200 μl of culture medium without serum were added to Transwell inserts (Transwell culture inserts, pore size of 8 μm; Corning, 3422), and 800 μl of culture supernatant from each of the three groups was added to the lower Transwell chamber. The HUVECs were cultivated in a cell culture incubator for 20 hours. The cells were then fixed in methanol and stained with crystal violet solution (0.5%) at room temperature for 30 min. Cotton swabs were used to remove nonmigrated cells. The experiment was performed in triplicate. The transmigrated cells were photographed (×200 magnification) with a Nikon Digital Sight DS-U2 (Nikon, Tokyo, Japan) camera attached to an Olympus BX50 microscope (Olympus Optical Co. Ltd., Tokyo, Japan). The total migrated HUVECs were quantified in five randomly selected HPFs. The HUVECs were purchased from the Shanghai Institutes for Biological Sciences of the Chinese Academy of Sciences. The H9C2 cells were purchased from the American Type Culture Collection (CRL1446, cardiac myoblasts from rats).

Animal surgery and echocardiographic assessment

Sprague-Dawley rats (male, 200 to 250 g) were obtained from the Shanghai Laboratory Animal Center. All procedures used in the study conformed to the Guide for the Care and Use of Laboratory Animals and were under the supervision of the Shanghai Jiao Tong University Institutional Animal Care and Use Committee. The Sprague-Dawley rats were anesthetized through intraperitoneal injection of pentobarbital sodium (30 mg/kg) and intubated with cannulas connected to a rodent ventilator. We previously applied MN patches to the skin by pressing with a thumb (at a force of 2.0 to 2.5 kg) (*20*). However, exertion of this heavy pressure to fix MNs on rat hearts while they are beating at 500 beats/min is difficult. Thus, a customized apparatus that operates via a principle similar to that of off-pump coronary aortic bypass grafting stabilizers (which provide stability during coronary revascularization surgery in patients suffering from CVD) was used for MN implantation (Fig. 1, A and C, and movies S1 and S3). The customized apparatus was a cylindrical conducting cavity with a backing plate. The inner and outer diameters were 9.2 and 10.3 mm, respectively. The inside cavity was 2.2 mm in height. An orifice (2.7 mm in diameter) was located in the center of the backing plate and was attached with a suction tube to a suction source. The MNs were attached to the backing plate with adhesive tape. There was a small gap (1.0 mm) between the hard backing of the MNs and the backing plate to ensure the patency of the cavity. When suction was provided, the targeted myocardial region entered the cavity of the customized apparatus. Consequently, MNs were passively and completely inserted into the soft myocardium. After stopping the supply of suction, the MNs detached from the backing plate and were maintained on the surface of the epicardium for 6 min. The negative pressure was ~−8 kPa (~−60 mmHg) at the time of MN application. The suction intensity (~−400 mmHg) applied to immobilize beating hearts during coronary artery bypass surgery is clinically safe and does not cause myocardial damage (*56*). In the DI group, 50 μl (~5×10^{10} vg) of AAV-GFP and AAV-VEGF, the same quantity of virus as that used in the MN-AAV group was injected into the left anterior wall in three equal aliquots using a 27-gauge needle via three injections into the predesignated area (*57*). The success of LAD ligation, which was used to induce the MI model, was confirmed by regional cyanosis of the anterior LV and an increase in the ST segment in the electrocardiogram (*26*). MN and MN-VEGF were implanted following MI. Echocardiographic measurements were taken for the four groups (the MI, MI + MN, MI + MN-VEGF, and MI + DI-VEGF groups) 2 days and 4 weeks after surgery. Isoflurane anesthesia was used to perform standard transthoracic echocardiography using an ultrasound imaging system (Vevo 2100 Imaging System, Visual Sonics, Toronto, ON, Canada). To assess cardiac function, echocardiographic data, including EF, FS, LVIDs, and LVIDd values, were collected and analyzed.

MN insertion and AAV delivery

Methylene blue– and FITC-AAV–loaded MNs were used to confirm the insertion of the MNs following application to target heart regions in vivo. For analysis of MN insertion, the delivery of methylene blue and FITC-AAV to precise regions of the heart was assessed by observing and quantifying the puncture spots in the epicardium and heart sections. MN-AAV-LUC were applied to the left anterior wall in normal rats and detected by an in vivo fluorescence imaging system after 4 weeks. The luciferase activity in the region of interest was analyzed after intraperitoneal injection of the XenoLight D-Luciferin - K^+ Salt bioluminescent substrate and detection with an in vivo bioluminescence imaging system (IVIS Spectrum, PerkinElmer, Waltham, MA, USA) 10 min after the injection of substrate.

Safety of the MN application in vivo

We compared the myocardial tissue density of CD68—a pan-macrophage marker-positive macrophages among the MN-AAV, DI-AAV, and NC groups 7 days after the AAV vectors were delivered to the myocardium. In addition, cardiac function was measured in the rats that received the MNs, and normal rats were used as controls.

Histochemical and immunohistochemical analysis

LV walls transfected with AAV-GFP and other rat organs, including the kidneys, lungs, liver, and skeletal muscles, were harvested at

the end of the functional experiments, embedded, and frozen in Tissue-Tek optimum cutting temperature compound. Then, the walls were cryosectioned horizontally at an 8-μm thickness, and 4% paraformaldehyde was applied to fix the heart samples for 3 days at 4°C. The fixed tissues were embedded in paraffin and sectioned at a thickness of 4 μm. The sections were placed onto slides and used for picrosirius red, HE, Masson's trichrome, and immunofluorescence staining. WB assays were performed with standard WB techniques, as previously described (*58*), and the antigen-antibody reactions were visualized by enhanced chemiluminescence (Thermo Fisher Scientific, Rockford, IL, USA). The antibodies used in the current study are shown in table S1. Quantification was performed by densitometry. Independent experiments were repeated in triplicate. The tissue sections were stained with primary antibodies and then incubated with fluorescent secondary antibodies. The fluorescent images were acquired under a Zeiss LSM 700 confocal microscope or a fluorescence microscope.

Serum VEGF levels

For analysis of variations in serum VEGF, blood samples were collected from the MI and MI + MN-VEGF groups 0, 1, 2, 3, and 4 weeks after LAD ligation. The levels of serum VEGF were detected with an enzyme-linked immunosorbent assay (ELISA) kit for human VEGF (R&D Systems) according to a standard protocol and the manufacturer's specifications. The samples were measured in duplicate.

Statistical analysis

Statistical analysis was performed using IBM SPSS software version 23.0. The data are presented as the means ± SD. The P values were calculated using one-way analysis of variance (ANOVA) with post hoc least significant difference multiple comparison tests to compare four groups or Student's t test to compare two groups. The criterion of statistical significance was set at $P < 0.05$ ($^{*}P < 0.05$, $^{**}P < 0.01$, $^{***}P < 0.001$, and $^{****}P < 0.0001$).

SUPPLEMENTARY MATERIALS

Supplementary material for this article is available at http://advances.sciencemag.org/cgi/content/full/6/25/eaaz3621/DC1

View/request a protocol for this paper from *Bio-protocol*.

REFERENCES AND NOTES

1. Writing Group Members, D. Mozaffarian, E. J. Benjamin, A. S. Go, D. K. Arnett, M. J. Blaha, M. Cushman, S. R. Das, S. de Ferranti, J.-P. Després, H. J. Fullerton, V. J. Howard, M. D. Huffman, C. R. Isasi, M. C. Jiménez, S. E. Judd, B. M. Kissela, J. H. Lichtman, L. D. Lisabeth, S. Liu, R. H. Mackey, D. J. Magid, D. K. McGuire, E. R. Mohler, C. S. Moy, P. Muntner, M. E. Mussolino, K. Nasir, R. W. Neumar, G. Nichol, L. Palaniappan, D. K. Pandey, M. J. Reeves, C. J. Rodriguez, W. Rosamond, P. D. Sorlie, J. Stein, A. Towfighi, T. N. Turan, S. S. Virani, D. Woo, R. W. Yeh, M. B. Turner; American Heart Association Statistics Committee; Stroke Statistics Subcommittee, Heart disease and stroke statistics—2016 update. *Circulation* **133**, e38–e360 (2016).
2. J. Tang, J. Wang, K. Huang, Y. Ye, T. Su, L. Qiao, M. T. Hensley, T. G. Caranasos, J. Zhang, Z. Gu, K. Cheng, Cardiac cell-integrated microneedle patch for treating myocardial infarction. *Sci. Adv.* **4**, eaat9365 (2018).
3. H. Wang, C. B. Rodell, M. E. Lee, N. N. Dusaj, R. J. Gorman, J. A. Burdick, R. C. Gorman, J. F. Wenk, Computational sensitivity investigation of hydrogel injection characteristics for myocardial support. *J. Biomech.* **64**, 231–235 (2017).
4. M. R. Afzal, A. Samanta, Z. I. Shah, V. Jeevanantham, A. Abdel-Latif, E. K. Zuba-Surma, B. Dawn, Adult bone marrow cell therapy for ischemic heart disease: Evidence and insights from randomized controlled trials. *Circ. Res.* **117**, 558–575 (2015).
5. H. K. Awada, M. P. Hwang, Y. Wang, Towards comprehensive cardiac repair and regeneration after myocardial infarction: Aspects to consider and proteins to deliver. *Biomaterials* **82**, 94–112 (2016).
6. D. Zhao, P. Feng, Y. Sun, Z. Qin, Z. Zhang, Y. Tan, E. Gao, W. B. Lau, X. Ma, J. Yang, S. Yu, X. Xu, D. Yi, W. Yi, Cardiac-derived CTRP9 protects against myocardial ischemia/reperfusion injury via calreticulin-dependent inhibition of apoptosis. *Cell Death Dis.* **9**, 723 (2018).
7. H. Zhu, X. Jiang, X. Li, M. Hu, W. Wan, Y. Wen, Y. He, X. Zheng, Intramyocardial delivery of VEGF165 via a novel biodegradable hydrogel induces angiogenesis and improves cardiac function after rat myocardial infarction. *Heart Vessel.* **31**, 963–975 (2016).
8. S. Kawamoto, Q. Shi, Y. Nitta, J. Miyazaki, M. D. Allen, Widespread and early myocardial gene expression by adeno-associated virus vector type 6 with a β-actin hybrid promoter. *Mol. Ther.* **11**, 980–985 (2005).
9. U. Nussinovitch, L. Gepstein, Optogenetics for in vivo cardiac pacing and resynchronization therapies. *Nat. Biotechnol.* **33**, 750–754 (2015).
10. K. M. Prasad, Y. Xu, Z. Yang, M. C. Toufektsian, S. S. Berr, B. A. French, Topoisomerase inhibition accelerates gene expression after adeno-associated virus-mediated gene transfer to the mammalian heart. *Mol. Ther.* **15**, 764–771 (2007).
11. N. Smart, S. Bollini, K. N. Dubé, J. M. Vieira, B. Zhou, S. Davidson, D. Yellon, J. Riegler, A. N. Price, M. F. Lythgoe, W. T. Pu, P. R. Riley, De novo cardiomyocytes from within the activated adult heart after injury. *Nature* **474**, 640–644 (2011).
12. J. M. Collins, B. Russell, Stem cell therapy for cardiac repair. *J. Cardiovasc. Nurs.* **24**, 93–97 (2009).
13. S.-J. Park, R. Y. Kim, B.-W. Park, S. Lee, S. W. Choi, J.-H. Park, J. J. Choi, S.-W. Kim, J. Jang, D.-W. Cho, H.-M. Chung, S.-H. Moon, K. Ban, H.-J. Park, Dual stem cell therapy synergistically improves cardiac function and vascular regeneration following myocardial infarction. *Nat. Commun.* **10**, 3123 (2019).
14. K. Ishikawa, T. Weber, R. J. Hajjar, Human cardiac gene therapy. *Circ. Res.* **123**, 601–613 (2018).
15. K. Gabisonia, G. Prosdocimo, G. D. Aquaro, L. Carlucci, L. Zentilin, I. Secco, H. Ali, L. Braga, N. Gorgodze, F. Bernini, S. Burchielli, C. Collesi, L. Zandona, G. Sinagra, M. Piacenti, S. Zacchigna, R. Bussani, F. A. Recchia, M. Giacca, MicroRNA therapy stimulates uncontrolled cardiac repair after myocardial infarction in pigs. *Nature* **569**, 418–422 (2019).
16. R. J. Hajjar, K. Ishikawa, Introducing genes to the heart: All about delivery. *Circ. Res.* **120**, 33–35 (2017).
17. X. Xiao, J. Li, R. J. Samulski, Efficient long-term gene transfer into muscle tissue of immunocompetent mice by adeno-associated virus vector. *J. Virol.* **70**, 8098–8108 (1996).
18. P. D. Kessler, G. M. Podsakoff, X. Chen, S. A. McQuiston, P. C. Colosi, L. A. Matelis, G. J. Kurtzman, B. J. Byrne, Gene delivery to skeletal muscle results in sustained expression and systemic delivery of a therapeutic protein. *Proc. Natl. Acad. Sci. U.S.A.* **93**, 14082–14087 (1996).
19. C. Qiao, Z. Yuan, J. Li, B. He, H. Zheng, C. Mayer, J. Li, X. Xiao, Liver-specific microRNA-122 target sequences incorporated in AAV vectors efficiently inhibits transgene expression in the liver. *Gene Ther.* **18**, 403–410 (2011).
20. S. Yang, F. Wu, J. Liu, G. Fan, W. Welsh, H. Zhu, T. Jin, Phase-transition microneedle patches for efficient and accurate transdermal delivery of insulin. *Adv. Funct. Mater.* **25**, 4633–4641 (2015).
21. S. Coulman, C. Allender, J. Birchall, Microneedles and other physical methods for overcoming the stratum corneum barrier for cutaneous gene therapy. *Crit. Rev. Ther. Drug Carrier Syst.* **23**, 205–258 (2006).
22. S. Hirobe, H. Azukizawa, T. Hanafusa, K. Matsuo, Y. S. Quan, F. Kamiyama, I. Katayama, N. Okada, S. Nakagawa, Clinical study and stability assessment of a novel transcutaneous influenza vaccination using a dissolving microneedle patch. *Biomaterials* **57**, 50–58 (2015).
23. J. Yu, Y. Zhang, Y. Ye, R. DiSanto, W. Sun, D. Ranson, F. S. Ligler, J. B. Buse, Z. Gu, Microneedle-array patches loaded with hypoxia-sensitive vesicles provide fast glucose-responsive insulin delivery. *Proc. Natl. Acad. Sci. U.S.A.* **112**, 8260–8265 (2015).
24. J. Yu, J. Wang, Y. Zhang, G. Chen, W. Mao, Y. Ye, A. R. Kahkoska, J. B. Buse, R. Langer, Z. Gu, Glucose-responsive insulin patch for the regulation of blood glucose in mice and minipigs. *Nat. Biomed. Eng.* **4**, 499–506 (2020).
25. J. Wang, Z. Wang, J. Yu, A. R. Kahkoska, J. B. Buse, Z. Gu, Glucose-responsive insulin and delivery systems: Innovation and translation. *Adv. Mater.* **32**, e1902004 (2019).
26. Y. Yang, D. Lei, S. Huang, Q. Yang, B. Song, Y. Guo, A. Shen, Z. Yuan, S. Li, F. L. Qing, X. Ye, Z. You, Q. Zhao, Elastic 3D-printed hybrid polymeric scaffold improves cardiac remodeling after myocardial infarction. *Adv. Healthc. Mater.* **8**, e1900065 (2019).
27. J. H. Kim, Y. Jung, S.-H. Kim, K. Sun, J. Choi, H. C. Kim, Y. Park, S. H. Kim, The enhancement of mature vessel formation and cardiac function in infarcted hearts using dual growth factor delivery with self-assembling peptides. *Biomaterials* **32**, 6080–6088 (2011).
28. J.-D. Schwalm, M. McKee, M. D. Huffman, S. J. C. Yusuf, Resource effective strategies to prevent and treat cardiovascular disease. *Circulation* **133**, 742–755 (2016).
29. P. M. Grossman, Z. Han, M. Palasis, J. J. Barry, R. J. Lederman, Incomplete retention after direct myocardial injection. *Catheter. Cardiovasc. Interv.* **55**, 392–397 (2002).

30. C. J. Teng, J. Luo, R. C. J. Chiu, D. Shum-Tim, Massive mechanical loss of microspheres with direct intramyocardial injection in the beating heart: Implications for cellular cardiomyoplasty. *J. Thorac. Cardiovasc. Surg.* **132**, 628–632 (2006).
31. D. Hou, A.-S. Youssef Eyas, J. Brinton Todd, P. Zhang, P. Rogers, T. Price Erik, C. Yeung Alan, H. Johnstone Brian, G. Yock Paul, L. March Keith, Radiolabeled cell distribution after intramyocardial, intracoronary, and interstitial retrograde coronary venous delivery. *Circulation* **112**, I150–I156 (2005).
32. Z. Tao, B. Chen, X. Tan, Y. Zhao, L. Wang, T. Zhu, K. Cao, Z. Yang, Y. W. Kan, H. Su, Coexpression of VEGF and angiopoietin-1 promotes angiogenesis and cardiomyocyte proliferation reduces apoptosis in porcine myocardial infarction (MI) heart. *Proc. Natl. Acad. Sci. U.S.A.* **108**, 2064–2069 (2011).
33. R. J. Lee, M. L. Springer, W. E. Blanco-Bose, R. Shaw, P. C. Ursell, H. M. J. C. Blau, VEGF gene delivery to myocardium: Deleterious effects of unregulated expression. *Circulation* **102**, 898–901 (2000).
34. T. D. Henry, B. H. Annex, G. R. McKendall, M. A. Azrin, J. J. Lopez, F. J. Giordano, P. Shah, J. T. Willerson, R. L. Benza, D. S. Berman, C. M. Gibson, A. Bejamonde, A. C. Rundle, J. Fine, E. R. McCluskey; VIVA Investigators, The VIVA trial: Vascular endothelial growth factor in ischemia for vascular angiogenesis. *Circulation* **107**, 1359–1365 (2003).
35. T. Johnson, L. Zhao, G. Manuel, H. Taylor, D. Liu, Approaches to therapeutic angiogenesis for ischemic heart disease. *J. Mol. Med.* **97**, 141–151 (2019).
36. J.-S. Choi, K.-B. Kim, W. Han, D. S. Kim, J. S. Park, J. J. Lee, D. S. Lee, Efficacy of therapeutic angiogenesis by intramyocardial injection of pCK-VEGF165 in pigs. *Ann. Thorac. Surg.* **82**, 679–686 (2006).
37. G. Vera Janavel, A. Crottogini, P. Cabeza Meckert, L. Cuniberti, A. Mele, M. Papouchado, N. Fernández, A. Bercovich, M. Criscuolo, C. Melo, R. Laguens, Plasmid-mediated VEGF gene transfer induces cardiomyogenesis and reduces myocardial infarct size in sheep. *Gene Ther.* **13**, 1133–1142 (2006).
38. M. Ferrarini, N. Arsic, F. A. Recchia, L. Zentilin, S. Zacchigna, X. Xu, A. Linke, M. Giacca, T. H. Hintze, Adeno-associated virus-mediated transduction of VEGF165 improves cardiac tissue viability and functional recovery after permanent coronary occlusion in conscious dogs. *Circ. Res.* **98**, 954–961 (2006).
39. K. Kukuła, A. Urbanowicz, M. Kłopotowski, M. Dąbrowski, J. Pręgowski, J. Kądziela, Z. Chmielak, A. Witkowski, W. Rużyłło, Long-term follow-up and safety assessment of angiogenic gene therapy trial VIF-CAD: Transcatheter intramyocardial administration of a bicistronic plasmid expressing VEGF-A165/bFGF cDNA for the treatment of refractory coronary artery disease. *Am. Heart J.* **215**, 78–82 (2019).
40. H. Matsuno, O. Kozawa, N. Yoshimi, S. Akamatsu, A. Hara, H. Mori, K. Okada, S. Ueshima, O. Matsuo, T. Uematsu, Lack of α2-antiplasmin promotes pulmonary heart failure via overrelease of VEGF after acute myocardial infarction. *Blood* **100**, 2487–2493 (2002).
41. E. R. Schwarz, M. T. Speakman, M. Patterson, S. S. Hale, J. M. Isner, L. H. Kedes, R. A. Kloner, Evaluation of the effects of intramyocardial injection of DNA expressing vascular endothelial growth factor (VEGF) in a myocardial infarction model in the rat–Angiogenesis and angioma formation. *J. Am. Coll. Cardiol.* **35**, 1323–1330 (2000).
42. H. L. Quinn, M. C. Kearney, A. J. Courtenay, M. T. McCrudden, R. F. Donnelly, The role of microneedles for drug and vaccine delivery. *Expert Opin. Drug Deliv.* **11**, 1769–1780 (2014).
43. K. Y. Seong, M. S. Seo, D. Y. Hwang, E. D. O'Cearbhaill, S. Sreenan, J. M. Karp, S. Y. Yang, A self-adherent, bullet-shaped microneedle patch for controlled transdermal delivery of insulin. *J. Control. Release* **265**, 48–56 (2017).
44. A. Ullah, H. Khan, H. J. Choi, G. M. Kim, Smart microneedles with porous polymer coatings for pH-responsive drug delivery. *Polymers* **11**, E1834 (2019).
45. S.-H. Baek, J.-H. Shin, Y.-C. Kim, Drug-coated microneedles for rapid and painless local anesthesia. *Biomed. Microdevices* **19**, 2 (2017).
46. A. V. Romanyuk, V. N. Zvezdin, P. Samant, M. I. Grenader, M. Zemlyanova, M. R. Prausnitz, Collection of analytes from microneedle patches. *Anal. Chem.* **86**, 10520–10523 (2014).
47. Z.-F. Zhong, P.-M. Hoi, G.-S. Wu, Z.-T. Xu, W. Tan, X.-P. Chen, L. Cui, T. Wu, Y.-T. Wang, Anti-angiogenic effect of furanodiene on HUVECs in vitro and on zebrafish in vivo. *J. Ethnopharmacol.* **141**, 721–727 (2012).
48. J. Guo, G. S. Lin, C. Y. Bao, Z. M. Hu, M. Y. Hu, Anti-inflammation role for mesenchymal stem cells transplantation in myocardial infarction. *Inflammation* **30**, 97–104 (2007).
49. L. Zangi, K. O. Lui, A. von Gise, Q. Ma, W. Ebina, L. M. Ptaszek, D. Später, H. Xu, M. Tabebordbar, R. Gorbatov, B. Sena, M. Nahrendorf, D. M. Briscoe, R. A. Li, A. J. Wagers, D. J. Rossi, W. T. Pu, K. R. Chien, Modified mRNA directs the fate of heart progenitor cells and induces vascular regeneration after myocardial infarction. *Nat. Biotechnol.* **31**, 898–907 (2013).
50. R. Pan, Y. Dai, X.-H. Gao, D. Lu, Y.-F. Xia, Inhibition of vascular endothelial growth factor-induced angiogenesis by scopoletin through interrupting the autophosphorylation of VEGF receptor 2 and its downstream signaling pathways. *Vasc. Pharmacol.* **54**, 18–28 (2011).
51. X. Wang, L. Wang, Q. Wu, F. Bao, H. Yang, X. Qiu, J. Chang, Chitosan/calcium silicate cardiac patch stimulates cardiomyocyte activity and myocardial performance after infarction by synergistic effect of bioactive ions and aligned nanostructure. *ACS Appl. Mater. Interfaces* **11**, 1449–1468 (2019).
52. R. F. Donnelly, K. Mooney, M. T. McCrudden, E. M. Vicente-Perez, L. Belaid, P. Gonzalez-Vazquez, J. C. McElnay, A. D. Woolfson, Hydrogel-forming microneedles increase in volume during swelling in skin, but skin barrier function recovery is unaffected. *J. Pharm. Sci.* **103**, 1478–1486 (2014).
53. K. Tsioris, W. K. Raja, E. M. Pritchard, B. Panilaitis, D. L. Kaplan, F. G. Omenetto, Fabrication of silk microneedles for controlled-release drug delivery. *Adv. Funct. Mater.* **22**, 330–335 (2012).
54. T. Y. Tsui, C. K. Lau, J. Ma, X. Wu, Y. Q. Wang, S. Farkas, R. Xu, H. J. Schlitt, S. T. Fan, rAAV-mediated stable expression of heme oxygenase-1 in stellate cells: A new approach to attenuate liver fibrosis in rats. *Hepatology* **42**, 335–342 (2005).
55. U.-P. Rohr, M.-A. Wulf, S. Stahn, U. Steidl, R. Haas, R. Kronenwett, Fast and reliable titration of recombinant adeno-associated virus type-2 using quantitative real-time PCR. *J. Virol. Methods* **106**, 81–88 (2002).
56. E. W. L. Jansen, C. Borst, J. R. Lahpor, P. F. Grundeman, F. D. Eefting, A. Nierich, E. O. R. de Medina, J. J. Bredee, Coronary artery bypass grafting without cardiopulmonary bypass using the octopus method: Results in the first one hundred patients. *J. Thorac. Cardiovasc. Surg.* **116**, 60–67 (1998).
57. X. Gu, Y. Matsumura, Y. Tang, S. Roy, R. Hoff, B. Wang, W. R. Wagner, Sustained viral gene delivery from a micro-fibrous, elastomeric cardiac patch to the ischemic rat heart. *Biomaterials* **133**, 132–143 (2017).
58. Z. Q. Wang, C. Y. He, L. Hu, H. P. Shi, J. F. Li, Q. L. Gu, L. P. Su, B. Y. Liu, C. Li, Z. Zhu, Long noncoding RNA UCA1 promotes tumour metastasis by inducing GRK2 degradation in gastric cancer. *Cancer Lett.* **408**, 10–21 (2017).

Acknowledgments

Funding: This work was supported by grants from the National Natural Science Foundation of China (81671832, 81571826, and 81690262), the Natural Science Foundation of Shanghai (18ZR1401900), the Shanghai Municipal Education Commission—Gaofeng Clinical Medicine Grant Support (826158), and the Shanghai Municipal Key Clinical Specialty Construction Project. **Author contributions:** H.S. and T.X. contributed equally to this work. H.S., T.X., T.J., F.W., X.Y., and Q.Z. designed the research. H.S., T.X., C.J., S.H., Q.Y., and Y.Y. performed the cellular and animal experiments, analyzed the data, and drafted the paper. D.L. and Z.Y. performed the test of mechanical properties. Q.Z., X.Y., F.W., and T.J. directed and supervised the study. All authors contributed to the scientific discussions, data interpretation, and the manuscript. **Competing interests:** The authors declare that they have no competing interests. **Data and materials availability:** All data needed to evaluate the conclusions in the paper are present in the paper and/or the Supplementary Materials. Additional data related to this paper may be requested from the authors.

Submitted 11 September 2019
Accepted 4 May 2020
Published 17 June 2020
10.1126/sciadv.aaz3621

Citation: H. Shi, T. Xue, Y. Yang, C. Jiang, S. Huang, Q. Yang, D. Lei, Z. You, T. Jin, F. Wu, Q. Zhao, X. Ye, Microneedle-mediated gene delivery for the treatment of ischemic myocardial disease. *Sci. Adv.* **6**, eaaz3621 (2020).